Chinese Chemical Letters 32 (2021) 3265–3276

Contents lists available at ScienceDirect

Chinese Chemical Letters

journal homepage: www.elsevier.com/locate/cclet

Review

Recent advances in BiOBr-based photocatalysts for environmental remediation

Lingyou Meng, Yang Qu*, Liqiang Jing*

Key Laboratory of Functional Inorganic Materials Chemistry, School of Chemistry and Material Sciences, Heilongjiang University, Harbin 150080, China

ARTICLE INFO

Article history:
Received 8 February 2021
Received in revised form 17 March 2021
Accepted 30 March 2021
Available online 2 April 2021

Keywords:
BiOBr
Visible-light photocatalysis
Electron modulation
Charge separation
Environmental remediation

ABSTRACT

The efficient utilization of solar energy through photocatalysis is ideal for solving environmental issues and the development sustainable future. BiOBr-based semiconductors possess unique narrowed bandgaps and layered structures, thereby widely studied as photocatalysts for environmental remediation. However, a little has been focused on the comprehensive reviewing of BiOBr despite its extensive and promising applications. In this review, the state-of-the-art developments of BiOBr-based photocatalysts for environmental remediation are summarized. Particular focus is paid to the synthetic strategies for the control of the resulting morphologies, as well as efficient modification strategies for improving the photocatalytic activities. These include boosting the bulk phase by charge separation, enhancing the spatial charge separation, and engineering the surface states. The environmental uses of BiOBr-based photocatalysts are also reviewed in terms of purification of pollutants and CO_2 reduction. Finally, future challenges and opportunities of BiOBr-based materials in photocatalysis are discussed. Overall, this review provides a good basis for future exploration of high-efficiency solar-driven photocatalysts for environmental sustainability.

1. Introduction

Environmental protection strategies are being developed to cope with the current issues generated by the rapidly developing society, which brings more environmental waste far exceeding the tolerable capacity. Semiconductor photocatalysts are promising materials due to their environmentally friendly and energy-saving features coupled with their highly effective synthetic approaches [1,2]. The mechanism of photocatalysis by semiconductors involves both photophysical and surface catalytic science processes. As shown in Fig. 1, the absorption of light by the semiconductor catalyst with sufficient energy excites electrons from the valence band (VB) to the conduction band (CB), leaving photogenerated holes with oxidation potential. In this process, large amounts of electrons will quickly recombine with electrons due to their short lifetimes. This makes the charge separation between electrons and holes a very important process in photocatalysis. As a result, tremendous efforts have been devoted to the separation between electrons and holes to participate in the subsequent redox reactions using built-in electric field, interface electric field, potential difference, and free diffusion. The separated electrons and holes possessing thermodynamic energies could then react with absorbed reactants on target surfaces. During these processes, holes may directly or indirectly participate in the reaction by generating hydroxyl radicals or hydroxylation of electrons with oxygen to induce reactive oxygen species for subsequent reactions.

Photocatalysis remains one of the effective ways to solve the current impending environmental and energy problems using clean and renewable solar energy [3]. In this process, sunlight is converted into chemical or electrical energy for sustainable development. During photocatalysis, active substances with strong oxidation ability are produced, including holes, superoxide radicals, and hydroxyl radicals. Such oxidizing species could efficiently convert harmful organic pollutants into small molecular substances with low toxicity without secondary pollution to the environment, making photocatalysis by semiconductors very up-and-coming environmental remediation technology. Furthermore, photocatalysis requires mild and stable reaction conditions, thereby easy to manage with highly practical usage value. Therefore, more attention has been focused on the development of high-efficiency photocatalysts, as well as gaining a better understanding of the photocatalytic mechanism. However, despite the progress, many aspects still require in-depth studies.

The development of efficient semiconductor photocatalysts has always been the focus of science and technology. Many materials

---

* Corresponding authors.
E-mail addresses: quyang@hlju.edu.cn (Y. Qu), jinglq@hlju.edu.cn (L. Jing).

https://doi.org/10.1016/j.cclet.2021.03.083

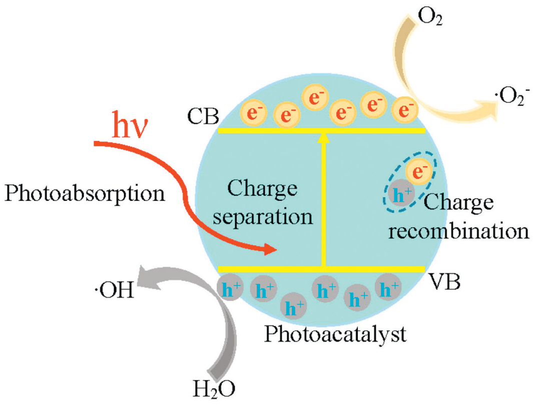

Fig. 1. Basic principle of semiconductor photocatalysis.

have so far demonstrated photocatalytic activities, including metal oxides (such as TiO_2 [4], ZnO [5] and SnO_2 [6]), metal sulfides (such as ZnS [7], MoS_2 [8], and CdS [9]), perovskite photocatalysts (such as $CH_3NH_3PbI_3$ [10], $BiFeO_3$ [11] and $SrTiO_3$ [12]), bismuth-based photocatalysts (such as BiOX, where X = Cl, Br and I [13,14], $BiVO_4$ [15] and Bi_2WO_6 [16]), silver-based photocatalysts (such as Ag_3PO_4 [17] and AgX, where X = Cl, Br and I [18,19]), polymer-like photocatalysts (such as g-C_3N_4 [20]), Organic polymers and conductive polymers (such as PANI [21]) and other materials (such as MOFs [22] and COFs [23]). Among these, TiO_2 is the most widely applied semiconductor photocatalyst due to its good chemical stability, low-cost, and non-toxicity. However, TiO_2 only responds under ultraviolet (UV) light and cannot maximize the utilization of solar energy, thereby greatly limiting the solar utilization efficiency [24]. Thus, finding efficient photocatalysts with a wide light response, enhanced charge separation, and strong surface catalytic capacity is of great interest to photocatalysis.

The solar spectrum is made of only ~5% UV light but nearly 47% is visible light, making the development of visible-light response photocatalysts useful. From the physics viewpoint, semiconductors with narrow bandgaps could respond to visible light. Until now, numerous semiconductors have been synthesized and found to possess photocatalytic activities. However, their narrow bandgaps make the photogenerated carriers easy to recombine. Besides, the comparable positive CB potentials render the photoelectrons thermodynamically insufficient for reduction.

Very recently, BiOBr with a narrow bandgap of 2.7–2.9 eV has attracted increasing attention as an alternative photocatalyst owing to its superior visible-light absorption, low toxicity, and high photocatalytic activity [25]. BiOBr is a typical V-VI-VII ternary p-type semiconductor with the conduction-band minimum (CBM) and valence-band maximum (VBM) located in different positions (as shown by density functional theory (DFT)) [26,27]. This provides BiOBr with an indirect bandgap semiconductor feature. In this respect, the BiOBr electron density of states calculations suggested O 2p and Br 4p as the main contributing orbitals to VBM, with a small boost from Bi 6s orbitals to yield photogenerated holes with high mobility. Note that the hybridization of Bi 6p and O 2p or Br 4p states exists at the bottom and middle of VB. On the other hand, the CBM of BiOBr is mainly contributed by Bi 6p with small participation from Bi 6s orbitals [28,29]. Meanwhile, the upper part of CB in BiOBr is mainly composed of Br 4s states [30]. This special electronic structure of BiOBr, especially the presence of Bi 6s orbitals contributed from both the CB and VB induces high charge mobility and tunable electronic state, favoring elevated photoactivity [31].

BiOBr compounds are composed of Bi_2O_2 layers which interleave with two Br atom slabs crystallized into a PbFCl-type structure [32,33]. As shown in Fig. 2, Bi and O are connected within Bi_2O_2 layers *via* strong covalent bonding. By comparison, interactions between [BiOBr] monolayers, as well as Bi_2O_2 and Br layers are based on van der Waals forces to yield open and indirect transition crystal structures [34,35]. In BiOBr, the crystal structure is energetically and thermodynamically favorable for the formation of layered configurations comprised of many BiOBr monolayers, in which each monolayer consists of Bi_2O_2 and Br_2 layers. The open layered crystal structure provides ample space for the polarization of atoms and orbitals, leading to the formation of an internal electric field perpendicular to both Bi_2O_2 and Br_2 layers. Such layered structure helps to separate electrons from holes. Meanwhile, the larger space between Bi-O and Bilayers of BiOBr induces photoelectrons belonging to an indirect transition mode with enough light polarization space. The latter is advantageous to the electron-hole in terms of the separation of indirect transition.

Huang *et al.* BiOBr used BiOCl for environmental remediation in 2006 [36]. Afterward, Zhang's group systematically investigated the photocatalytic activity of BiOX-based materials. Since then, intense research has been carried out on BiOX-based photocatalysis [37]. Note that BiOBr is extensively studied in photocatalysis as an important bismuth oxyhalide. As shown in Fig. 3, the number of published reports related to BiOBr increases year after year. For instance, over 1100 papers have been published in the past ten years using BiOBr as a photocatalyst. This indicates the popularity of BiOBr in photocatalysis. Among papers, numerous reviews referring to BiOBr have so far been published. For instance, Huang *et al.* surveyed the emerging strategies for tailoring BiOCl, BiOBr and BiOI nanostructures for boosting their photocatalytic properties [38]. Guo *et al.* reviewed the progress made in designing and tuning of bismuth oxyhalide materials for boosting their solar energy conversion rates [39]. They also discussed the photocatalytic applications of bismuth oxyhalide-based photocatalysts in areas of oxygen evolution, hydrogen evolution, CO_2 reduction, nitrogen fixation, organic synthesis, and pollutant removal. However, only a few reviews have dealt with BiOBr among bismuth oxyhalides [40].

In particular, only a handful of reviews have focused on individual BiOBr-based photocatalysts. Meanwhile, the number of publications dealing with the advantages and photocatalytic performances of BiOBr-based photocatalysts has substantially increased. Therefore, comprehensively summarizing current works related to BiOBr-based photocatalytic materials would be of great significance for guiding the design and synthesis of future visible-light-driven photocatalytic materials with high efficiency. Hence, recently emerged strategies for enhancing charge

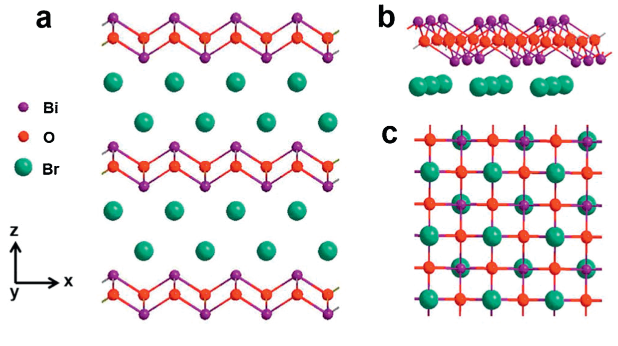

Fig. 2. Schematic diagrams of the laminar crystalline structure of BiOBr. (a) Front view, (b) Side view, and (c) Top view of BiOBr crystal unit cells. Reproduced with permission [34]. Copyright 2018, American Chemical Society.

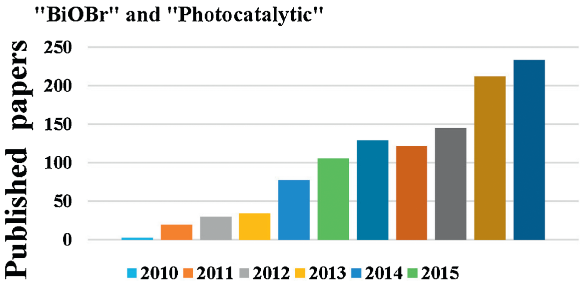

Fig. 3. Published papers in recent ten years obtained by using "BiOBr" and "Photocatalytic" as keywords in the web of science as of December 31, 2020.

separation and promoting the photoactivities are summarized in the present review.

2. Synthesis of nano-structured BiOBr

According to the structural characteristics and both physical and chemical properties, the synthesis of BiOBr materials with specific morphologies is still challenging. As shown in Fig. 4, BiOBr materials with different morphologies have been synthesized, such as zero dimension (0D), one-dimensional (1D), two-dimensional (2D) and three-dimensional (3D) structures [41]. Also, several methods have been developed for the synthesis of BiOBr, including hydro/solvothermal route, hydrolysis, precipitation, sol-gel, and microwave.

2.1. Hydro/solvothermal method

The hydrothermal method is a chemical reaction carried out in a sealed pressure vessel under high temperature and pressure using water as the solvent [42,43]. The powders obtained by the hydrothermal method are often characterized by good crystallinity without performing further sintering processes. The latter could effectively prevent grain growth and easy mixing of impurities during the sintering process. For instance, An *et al.* employed $Bi(NO_3)_3·5H_2O$ and KBr as raw materials to prepare BiOBr nanosheets by simple hydrothermal method at 160 °C for 12 h [44]. Huang *et al.* developed an improved hydrothermal route based on precipitation strategy. In this process, $Bi(NO_3)_3·5H_2O$ solution was first mixed with KBr solution followed by heating of the obtained suspension in an autoclave at 120 °C for 24 h to yield BiOBr plates with thicknesses around 10–100 nm [45]. Wang *et al.* employed the hydrothermal reaction at 160 °C for 12 h to synthesize BiOBr nanosheets with different exposed crystal faces [46]. In this process, $Bi(NO_3)_3·5H_2O$ and KBr were dissolved in dilute HNO_3 aqueous solution one after another. The pH value of the solution was adjusted by dropping an NaOH solution. Zhao *et al.* noticed strong internal electric fields in BiOBr with main (110) burst exposed crystal plane [47]. The negatively charged [O] layer and positively charged [BiBr] layer may also be arranged alternately along the (110) direction to effectively separate the photoelectron-hole pairs along the (110) direction, leading to improved photocatalytic activity. Han *et al.* reported BiOBr with a mainly exposed surface (001) or (010) by changing pH during the hydrothermal method under acidic conditions. At pH 6, the adsorption of H^+ ions on O^- atom terminal (001) surface prevented the growth of the material in the direction of (001) plane, giving preference to this plane for higher intrinsic activity. At pH > 6, the growth of the surface (010) plane was found beneficial due to its elevated photooxidation activity [48].

Another synthesis route of BiOBr consists of the solvothermal method [49], which was developed based on the hydrothermal method. The difference between both relies on the used solvent. The hydrothermal method employs H_2O as a solvent, while the solvothermal method utilizes organic solvents. For reactions involving compounds sensitive to H_2O, the use of organic solvents may effectively prevent the reaction of reactants with H_2O, hydrolysis, or decomposition of unstable components. Huo *et al.* obtained flower-like nanospheres assembled from nanosheets *via* solvent-thermal method using ethylene glycol (EG) and isopropanol as solvents and sodium dodecyl benzene sulfonate (SDBS) as a surfactant [50]. The as-obtained flower-like nanospheres showed multilevel reflection under light, promoting light absorption and

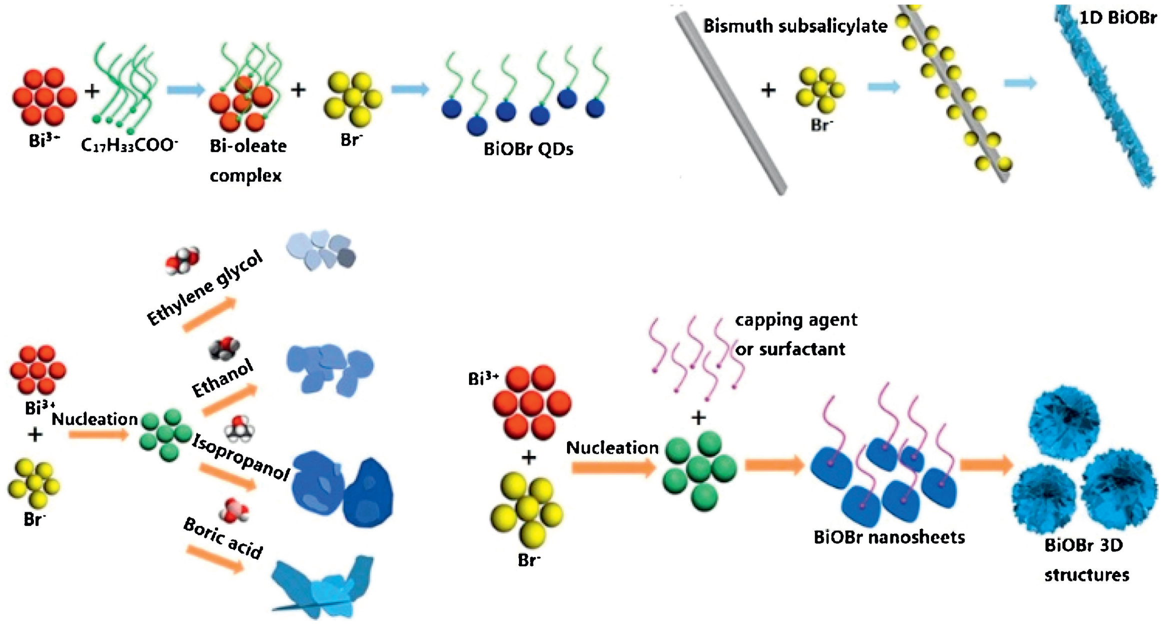

Fig. 4. Schematic illustration of the possible formation process of 0D BiOBr quantum dots, 1D, 2D and 3D BiOBr samples. Reproduced with permission [41]. Copyright 2020, Elsevier.

greatly improving the photocatalytic activity. Pu *et al.* synthesized 3D-flower BiOBr microspheres (diameter 2–6 mm) by the solvothermal method at 160 °C for 10 h [51]. An optimized BiOBr sample was obtained using EG as a solvent, $Bi(NO_3)_3{\cdot}5H_2O$ as Bi source, and hexadecyl trimethyl ammonium bromide (CTAB) as Br source. Lv *et al.* assembled BiOBr microflowers by the solvothermal method using $Bi(NO_3)_3{\cdot}5H_2O$ as Bi source, KBr as Br source, and EG as solvent [52]. In this process, the reactants were heated in an autoclave at 160 °C under autogenous pressure for 12 h to yield microflowers with diameters around 1 μm. Yang *et al.* successfully prepared BiOBr by the solvothermal method at 140 °C using reagents, such as $Bi(NO_3)_3{\cdot}5H_2O$, CTAB, 2-methoxyethanol, ethanol, and polyvinyl pyrrolidone (PVP) [53]. By changing the type of solvent and reaction time, hollow flower-like BiOBr, microspherical BiOBr, and micro-flower-like BiOBr were obtained. Zhao *et al.* synthesized BiOBr micron flowers with partially exposed (111) crystal surface plane by a simple solvent-thermal method using sodium dodecyl sulfate (SDS) as a sealing agent [54]. The as-obtained BiOBr with (111) crystal plane showed excellent electrochemical behavior and photocatalytic activity.

Both the hydrothermal and solvothermal processes are high-pressure liquid phase reactions of raw materials carried out in heated reactor. The closed reaction system allows the use of high temperature and high pressure, thereby facilitating the nucleation and crystallization.

2.2. Hydrolysis method

Hydrolysis is based on the decomposition of substances by H_2O or other media to form new substances. Hydrolysis is appropriate for mass production owing to its simple processing operation, available raw materials, economical, and environmentally friendly. In this process, $Bi(NO_3)_3{\cdot}5H_2O$ is often used as Bi source, during which Bi^{3+} cations react with H_2O to yield $BiONO_3$ and H^+ followed by reaction of Br^- with $BiONO_3$ to form Br-Bi-O-Bi-Br layer. Wu *et al.* reported a simple hydrolysis method based on $Bi(NO_3)_3{\cdot}5H_2O$ and NaBr. By adjusting the temperature and solvent without adding any surfactant or capper, BiOBr nanosheets with thicknesses ranging from 9 nm to 32 nm can easily form during the hydrolysis [55]. Guo *et al.* synthesized BiOBr quantum dots with diameters less than 5 nm by simple hydrolysis route at room temperature [41]. The resulting 0D BiOBr displayed high-performance photoactivity due to the presence of quantum dots by anchoring on the substrate, such as graphene or another crystalized photocatalyst. Fan *et al.* obtained 3D BiOBr photocatalyst by a facile one-step hydrolysis method under the conditions of pH 1 [56]. In this procedure, $Bi(NO_3)_3{\cdot}5H_2O$ and $NaBrO_3$ were first dissolved in distilled water. Next, Br source was added to Bi under continuous stirring and pH was adjusted to yield a resultant product after 3 h. Li *et al.* prepared a solution containing Br^- and H^+ by adjusting the pH value of NaBr solution to 2 through the addition of H_2SO_4 [57]. Afterward, Ti film loaded with Bi_2O_3 film was immersed in the solution to yield double-layered white BiOBr films deposited on the substrate Ti film through continuous hydrolysis of Bi_2O_3 film. The thickness of the flower-like layered BiOBr film was determined as 10 nm, and the plane size was 1.2 μm. The as-obtained double-layered structure did not only increase the surface area but also possessed higher light utilization efficiency due to the multiple reflections of the incident light. Guo *et al.* synthesized 1D BiOBr samples by a simple hydrolysis method.

Table 1
BiOBr photocatalysts prepared by different synthetic methods.

Sample	Synthesis method	Size	Ref.
BiOBr nanosheets	Hydrothermal method at 160 °C for 12 h.	Diameter of 1.5–2.7 μm and thickness of 150–300 nm.	[44]
BiOBr plates	Hydrothermal method at 120 °C for 24 h.	Widths of 1–2 mm and thickness of 10–100 nm.	[45]
BiOBr nanosheets	Hydrothermal method at 160 °C for 12 h.	Width of 1.5–3.5 mm and thickness of 100–200 nm.	[46]
Flower-like nanospheres	Solvent-thermal method using EG, isopropanol as solvents, and sodium SDBS as a surfactant at 160 °C for various times.	Diameter of 1.0–5.0 μm and thickness of 5–10 nm.	[50]
3D-flower BiOBr microspheres	Solvothermal method at 160 °C for 10 h and EG as a solvent.	Diameters of approximately 2–6 mm.	[51]
BiOBr microflowers	Solvothermal method using EG as solvent at 160 °C for 12 h.	Diameters around 1 μm.	[52]
Hollow flower-like BiOBr	Solvothermal method using 2-methoxyethanol and PVP at 140 °C for 0.5–12 h.	Outer diameter of 2.4 μm, shell thickness of 600 nm, and nanosheets thickness of 24 nm.	[53]
Micro-spherical BiOBr	Solvothermal method using 2-methoxyethanol at 140 °C for 0.5–12 h.	Microstructures assembled by the length of 600 nm and thickness of 70 nm BiOBr nanosheets.	[53]
Micro-flower-like BiOBr	Solvothermal method using ethanol and PVP at 140 °C for 24 h.	Diameter of 3 μm.	[53]
BiOBr micron flowers	Solvent-thermal method using SDS as a sealing agent at 120 °C for 8 h.	Microstructures of about 3 μm.	[54]
BiOBr nanosheets	Hydrolysis method by adjusting the temperature and solvent.	Thicknesses ranging from 9 nm to 32 nm.	[55]
BiOBr quantum dots	Hydrolysis method at room temperature.	Diameter less than 5 nm.	[41]
3D BiOBr	Hydrolysis method under pH 1.	Diameter of 6 μm.	[56]
Flower-like layered BiOBr films	Hydrolysis method in acidic condition.	Plane size of 1.2 μm and thickness of 10 nm.	[57]
1D BiOBr	Hydrolysis method for 10 min.	Average length and diameter of 2 μm and 220 nm.	[41]
BiOBr nanosheets	Chemical co-precipitation method for 1 h at 100 °C.	Yield heights of about 100 nm on the carrier.	[58]
BiOBr nanoparticles	Precipitation method using water/glycerol mixed solution.	A growth degree around 1 μm followed by assembly of 3D nanostructures with diameters of about 500 nm.	[59]
BiOBr nanoplates	Precipitation method by aging for 4 h.	Thicknesses of about 58 nm and sizes of 220–620 nm.	[60]
BiOBr microspheres	Non-hydrosol-gel method using $Bi(NO_3)_3$ and CTAB as precursors.	Diameters ranging from 2 to 5 μm.	[61]
BiOBr sheets	Sol-gel method using $Bi(NO_3)_3{\cdot}5H_2O$ and KBr as agents.	Size of 135–380 nm and thickness of 15–20 nm.	[62]
Flower-like BiOBr	Microwave-assistant method at 110 °C for 30 min.	Diameter of 200–300 nm.	[63]
Layered BiOBr microcubes	Microwave-assistant method at 160 °C for various times.	Uniform microcubes of 4 μm assembled by nanosheets with thicknesses less than 50 nm.	[64]
3D flower-like BiOBr	Microwave-assistant method at 200 W for 6 min.	Diameters of 4.79–5.48 μm.	[31]

The resulting hierarchy of BiOBr showed a rod-like shape with an average length and diameter of 2 μm and 220 nm, respectively. Also, the 1D BiOBr illustrated good photocatalytic performance toward the degradation of dyes [41].

2.3. Precipitation method

The precipitation method relies on dissolving all kinds of reactive substances in a solvent followed by a reaction to form insoluble compounds under certain conditions. The resulting precipitate is then subjected to appropriate heat treatment to obtain a final nanopowder. This route is advantageous in terms of simple processing and low-cost. For example, Wang *et al.* prepared BiOBr nanosheets by a chemical co-precipitation method using $Bi(NO_3)_3$ and KBr as Bi and Br precursors dissolved in deionized water, respectively [58]. The BiOBr precipitate was then formed by mixing two solutions for 1 h at 100 °C. The as-prepared BiOBr nanosheets were grown vertically on the carrier to yield heights around 100 nm. Zhang *et al.* assembled BiOBr nanoparticles using water/glycerol mixed solution as the solvent. The introduction of different proportions of glycerol into the reaction solution led to the control over the viscosity of the reaction system. In turn, the viscosity controlled the anisotropic growth of small BiOBr particles with a growth degree around 1 μm followed by assembly into 3D nanostructures with diameters around 500 nm [59]. Dong *et al.* obtained BiOBr nanoplates by dissolving KBr in an aqueous solution, and $Bi(NO_3)_3 \cdot 5H_2O$ in an aqueous acetic acid solution. Next, the KBr solution was added drop by drop to the mixture of $Bi(NO_3)_3$, and the resultant suspension was aged for 4 h to yield nanoplates with thicknesses around 58 nm and sizes of 220−620 nm [60].

2.4. Sol-gel route

The sol-gel process combining the hydrolytic precipitation is widely used to prepare nanomaterials by evenly mixing the reactants in a liquid phase environment. The dissolved precursors are then hydrolyzed and condensed to form a sol system followed by aging and polymerization to produce a gel. Finally, nanosized materials are obtained after drying and curing. Ai *et al.* assembled BiOBr microspheres by non-hydrosol-gel method using $Bi(NO_3)_3$ and CTAB as precursors [61]. The as-prepared BiOBr microspheres showed excellent catalytic activity and long-term stability thanks to their distinct hierarchical structures useful for the diffusion of NO oxidation intermediates and final products. Cai *et al.* synthesized BiOBr sheets by the sol-gel method using $Bi(NO_3)_3 \cdot 5H_2O$ and KBr as agents [62]. The BiOBr sheets and TiO_2 were coupled into BiOBr@TiO_2 heterojunction to effectively promoting the interface charge transfer and improving the separation efficiency of photogenerated electron holes. The resulting materials showed excellent photocatalytic activity and good decomposition performance of organic pollutants.

2.5. Microwave-assistant method

In the microwave assistant strategy, reactants undergo chemical reactions under microwave irradiation to produce desired nanomaterials. The microwave method is beneficial in terms of high thermal energy utilization rate, no pollution, rapid heating, and production of nanomaterials with uniform particle sizes. For example, Chen *et al.* dissolved $Bi(NO_3)_3 \cdot 5H_2O$, KBr, and CTAB in mannitol solution followed by placing the mixture in a microwave reactor at 110 °C for 30 min [63]. The precipitate was then washed and dried to yield flower-like BiOBr with great photocatalytic performances. Miao *et al.* prepared layered BiOBr microcubes by the microwave-assisted method using $Bi(NO_3)_3 \cdot 5H_2O$ and 1-hexadecyl-3-methylimidazolium-bromide as reactants [64]. The microcubes were self-assembled from lamellar BiOBr, leading to superior photocatalytic degradation activity, good stability, and strong mineralization ability under visible-light irradiation. Zhang *et al.* prepared BiF_3/BiOBr heterojunction photocatalyst by microwave-assisted reaction at 200 W for 6 min by adding an aqueous solution containing KBr and NaF to an acetic acid solution soluble in $Bi(NO_3)_3$ [31]. During the reaction, the presence of the catalyst accelerated the separation of photoelectrons and holes under visible light irradiation.

Table 1 summarizes the BiOBr synthesis methods. Among the above-discussed methods, the hydro/solvothermal reaction is the most used for the synthesis of BiOBr photocatalysts with different morphologies. Using this route, the exposed planes and vacancies may also be controlled during the synthesis. However, each method is still limited by some drawbacks, making the development of novel and effective methods for preparing BiOBr photocatalysts highly desirable to yield materials with enhanced charge separation and elevated activity.

3. Efficient strategies for promoting photoactivity

According to the photocatalytic mechanism, the photoactivities of BiOBr materials can be achieved by enhancing the charge separation and promoting the surface catalytic capacity. The insufficient utilization of photoelectron with low thermodynamic energy due to the existence of positive CB would result in poor charge separation for BiOBr. Another barrier to the charge separation has to do with bulk charge separation transfer [65]. Therefore, enhancing the charge separation through efficient strategies would significantly promote the photoactivity. Therefore, efficient strategies for improving the photoactivities of BiOBr

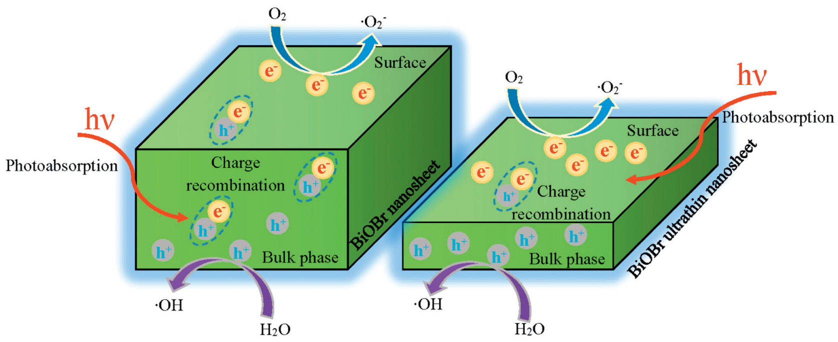

Fig. 5. Migration of photogenerated carriers in bulk BiOBr nanosheets and BiOBr ultrathin nanosheets.

are discussed in this review for better guidance. These include boosting the bulk phase charge transfer, enhancing the spatial charge separation, and engineering the surface states.

3.1. Boosting bulk phase charge transfer

3.1.1. Shortening diffusion distance through ultrathin 2D structure

During photocatalysis, photogenerated electrons and holes are excited in a few femtoseconds [66], and their migration from bulk to the surface active sites may take only hundreds of picoseconds. The recombination between electrons and holes takes from a few picoseconds to tens of nanoseconds. Particularly, the recombination of bulk phase of the catalyst takes only a few picoseconds, thereby much faster than both charge transport and charge consumption catalysis. Thus, most electrons and holes prefer to recombine in the photocatalyst body before reaching the surface [65]. To reduce the carrier recombination in bulk, photocatalysts with ultrathin 2D nanosheets like nanoflakes have been prepared. The influence of the space charge layer can be ignored due to thickness of nanosheets, which much thinner than the space charge layer. The photogenerated electrons and holes may then migrate from the interior or bulk to the surface by simple diffusion. Thinner nanosheets would require shorter migration distances for the propagation of electrons and holes from bulk to the surface [39]. As shown in Fig. 5, the recombination of electrons and holes in the bulk phase was effectively reduced, and the photocatalytic performance significantly improved [67]. Therefore, building ultrathin BiOBr nanosheets is effective for enhanced photocatalytic activities. In this view, Xia *et al.* assembled BiOBr nanosheets with average diameter of 200–300 nm and thickness of 3–4 nm [68]. The adjustment over the thickness of 2D nanosheets to several or one single layer led to a significant increase in the separation efficiency of photogenerated carriers during photocatalysts. As a result, shorter diffusion distances for electrons and holes transfer provided by ultrathin nanoflake structures inhibited the recombination of photoinduced electrons and holes, thereby effectively improving the photocatalytic performances. Liu *et al.* manufactured ultrathin 2D BiOBr nanosheets with thicknesses of less than 3 nm [69]. Compared to the contrast sample with a thickness of 25 nm, the ultrathin BiOBr showed a much higher photocatalytic activity.

3.1.2. Tuning of electronic structure through ion doping

Doping consists of adding impurities to semiconductors to generate or modify their electronic states [70,71]. Using doping elements, intermediate energy levels can be introduced into the semiconductor photocatalysts to tune their optical properties and energy band structures [72,73]. Additionally, doping influences the band structure by changing the Fermi level of the semiconductor. Thus, doping BiOBr affects the local electronic density to yield enlarged build-in electric fields, as well as improved bulk phase charge separation. This, in turn, would improve the photocatalytic activities of doped-semiconductor catalysts. Shao *et al.* inserted additional energy levels into the bandgap of BiOBr to produce a denser electron density around CB after doping with cobalt (Co) [74]. Under visible-light irradiation, the electrons in the VB of Co-doped BiOBr were excited to the Co-doped energy level to promote the formation of holes in VB. The electrons captured by the Co-doping level were further excited to CB and participate in the photocatalytic reaction. The existence of Co-doping energy level led to enhanced charge separation efficiency of Co-doped BiOBr, as well as widening of the spectral absorption range. As a result, the photocatalytic performances obviously improved. Wang *et al.* prepared homogeneous porous BiOBr microsphere photocatalysts doped with Ag^+ and Er^{3+} ions separately [75]. The diffusion of Ag into the BiOBr lattice led to the formation of the Schottky potential barrier, thereby spontaneously moving the photogenerated electrons toward Ag. The photogenerated electrons and holes became effectively separated, forming numerous holes on the catalyst surface, and thereby effectively improving the photocatalytic performances. On the other hand, Er^{3+} doping had also been used to increase the energy level of BiOBr, resulting in large numbers of photogenerated electrons and effective inhibition of recombined photogenerated electrons and holes. After capturing electrons from CB of BiOBr, Er^{3+} reduced doped Er^{3+} ions into Er^{2+}. Since Er^{2+} is unstable, it can easily release captured electrons to participate in the photocatalytic reaction. Consequently, Er^{3+} showed up-conversion performances. The existence of numerous new energy levels effectively improved the photocatalytic efficiencies. For example, Guo *et al.* prepared a Zn-doped BiOBr photocatalyst and noticed that doping of Zn can inhibit the recombination of photogenerated carriers [76]. Meanwhile, the band gap of Zn-doped BiOBr widened in the potential of VBM (more positive) and CBM (more negative), leading to higher redox chemical potentials of photogenerated carriers. Lv *et al.* prepared Cu-doped BiOBr photocatalyst by establishing the doped energy level in Cu-doped BiOBr bandgap [52]. The electrons in VB of Cu-doped BiOBr were transferred to the Cu-doped BiOBr energy level through the inter conversion process between Cu^+ and Cu^{2+}. Meanwhile, electrons in the VB of Cu-doped BiOBr and Cu-doped levels were excited to CB of Cu-doped BiOBr. Compared to bulk BiOBr, more photogenerated holes were generated, thereby effectively improving the photocatalytic performances of BiOBr. An *et al.* synthesized B-doped BiOBr nanosheets with unfilled electronic structure of B containing unpaired electrons as a good electron acceptor [44]. The electron-deficient nature of B was beneficial for acquiring an extra electron from VB, which then can be excited into CB of BiOBr to leave one extra hole in VB of BiOBr. Therefore, the presence of B in semiconductors can improve the separation efficiency of BiOBr for electron holes. Compared to pure BiOBr, B-doped BiOBr displayed higher oxidation capacity.

3.2. Enhancing spatial charge separation

3.2.1. Construction of traditional heterojunctions

Heterojunction structures are commonly utilized to produce a light-induced electron and hole separation. The use of interface electric fields may drive the directional spatial separation of photogenerated electrons and holes [77]. Formed heterojunctions would simultaneously promote the directional transfer of photogenerated electrons and holes at the heterojunction, as well as recombine photogenerated carriers. Therefore, the formation of heterojunctions may improve the photocatalytic performances more effectively than single photocatalysts [78]. Zhang *et al.* assembled a strong BiOI/BiOBr hetero-structure with tunable visible-light-driven photocatalytic reactivity [79]. The resulting BiOBr was excellent for the transfer of high-energy electrons by effectively slowing down the electron-hole recombination process to facilitate the photocatalytic reactions. Chen *et al. in-situ* grew graphitic carbon nitride ($g\text{-}C_3N_4$)/BiOBr heterojunctions, in which $g\text{-}C_3N_4$ nanosheets and BiOBr layer were formed on carbon fibers [80]. Under visible-light irradiation, the $g\text{-}C_3N_4$/BiOBr heterojunctions can be excited to generate electrons and holes due to the suitable band gap and the potential difference between both. Because the CB of $g\text{-}C_3N_4$ was much more negative than that of BiOBr, the photogenerated electrons in $g\text{-}C_3N_4$ at the CB band were easy to transfer to the CB of BiOBr across the intimate interface of well-aligned straddling band structures. Meanwhile, some produced holes in VB of BiOBr were prone to transfer to VB of $g\text{-}C_3N_4$, since VB in BiOBr was more positive than in $g\text{-}C_3N_4$. Xu *et al.* synthesized a magnetically recoverable BiOBr/Fe_3O_4 heterojunction photocatalyst with high photocatalytic activity. Since BiOBr was a p-type semiconductor photocatalyst while Fe_3O_4 was an n-type semiconductor photocatalyst, the formed p-n heterojunction produced an efficient charge separation to decline the recombination of photogenerated charge pairs [81].

3.2.2. Construction of uncommon heterojunctions

Since CB bottom of BiOBr is very positive, excited photoelectrons cannot thermodynamically produce reduction reactions, thereby increasing the recombination of photogenerated electrons and holes. The construction of traditional heterojunction has been used to drive the charge separation but electrons and holes with lost energies become thermodynamic useless for photocatalytic redox reactions. Studies based on semiconductor energy band theory and DFT calculations showed that empty orbitals in the bottom of CB could accept photogenerated electrons from VB through suitable energy excitation. In this process, excited electrons in oxides by appropriate visible-light photons will jump into high energy levels with sufficient energy to induce reduction reactions. However, such exciting high-level-energy electrons (HLEEs) at much higher energy levels would quickly return to the CB bottom (low energy levels) within picoseconds, making their use in following photocatalytic reactions difficult [82]. Therefore, separating and prolonging the lifetimes of HLEEs through the construction of appropriate electron energy platforms would achieve efficient photocatalysis.

Recently, Jing *et al.* employed surface photovoltage spectrometry (SPS) and photoelectrochemical measurements to demonstrate that co-modification by SnO_2 and Ag could significantly enhance electron-hole separation [83]. As shown in the photophysical results of Fig. 6, enhanced charge separation depended on the appropriate utilization of HLEEs upon CBM. In this process, SnO_2 with suitable CB potential was employed as a good platform to accept HLEEs of BiOBr before their relaxation into CB bottom, leading to an effective separation of HLEEs in CB of SnO_2. Meanwhile, the lifetime of photoelectrons was prolonged while the thermodynamic energy was maintained. Additionally, the co-modified Ag improved O_2 activation, further enhancing the charge separation. Wu *et al.* prepared heterojunction BiOBr/SnO_2 photocatalysts [84]. The theoretical calculations revealed that visible-light excitation only excited electrons in the VB of BiOBr into its CB, while SnO_2 remained in the ground state since it cannot be excited by visible light. The presence of the built-in electric field led to the migration of electrons from BiOBr to CB of SnO_2, while holes stayed in the VB of BiOBr to enable an efficient separation between electrons and holes. The resulting BiOBr/SnO_2 heterojunction exhibited excellent photocatalytic performances under visible light due to the efficient charge separation and longer carrier lifetime.

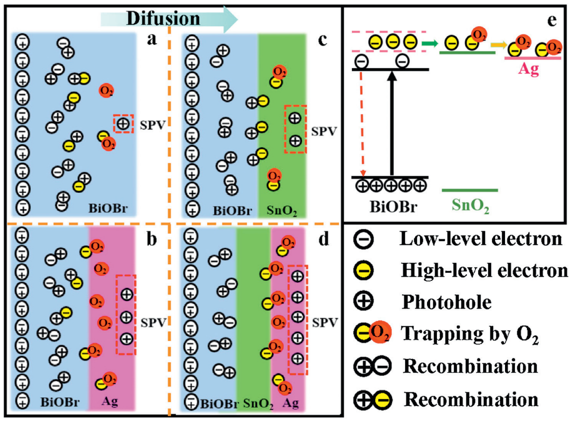

Fig. 6. The mechanisms of charge diffusion and trapping by adsorbed O_2 in different samples (a-d), as well as charge transfer and separation (e). Reproduced with permission [83]. Copyright 2020, Springer.

3.2.3. Construction of Z-Scheme heterojunction

Z-scheme photocatalysts combining two narrow-bandgap semiconductors are conducive to enhancing the charge separation and visible-light absorption [85]. Therefore, heterojunction nanocomposites are widely investigated in the past decades [86,87]. For example, Zhan *et al.* fabricated a Z-scheme heterojunction photocatalyst g-C_3N_4@polydopamine (PDA)/BiOBr (abbreviated as CNPB) with remarkably improved photocatalytic performances toward the degradation of sulfamethoxazole (SMX) under visible light irradiation [88]. Their radical scavenging and electron spin resonance (ESR) trapping experiments confirmed the occurrence of a Z-scheme charge transfer mechanism, in which holes and radical dot $^{\bullet}O^{2-}$ were determined as the major reactive species for oxidizing SMX. As shown in Fig. 7, the exposure of Z-type CNPB heterojunction to visible-light led to the transfer of photogenerated electrons in CB of BiOBr to the VB of g-C_3N_4 through PDA and binding to the holes. This process accumulated more electrons and holes in CB of g-C_3N_4 and VB of BiOBr, respectively. Sin *et al.* reported a new Z-type BiOBr/$MnFe_2O_4$ nanocomposite, in which spontaneous migration of photogenerated electron carriers promoted the separation of photogenerated electron holes and declined the recombination rate of photogenerated electron-hole pairs [89]. This, in turn, prolonged the carrier life of the photocatalytic reactions, as well as enhanced the photocatalytic performances of the catalyst. Wu *et al.* reported a 3D layered BiOBr/$BiOIO_3$ Z-type heterojunction, in which the formation of Z Scheme heterojunction promoted the separation and transfer efficiency of electron-hole pairs, as well as allowed the semiconductor to maintain its high redox power [90]. These features were conducive to the occurrence of redox reactions, as well as effectively improved photocatalytic performances. Mishra *et al.* synthesized CdS/BiOBr/$Bi_2O_2CO_3$ ternary heterostructural

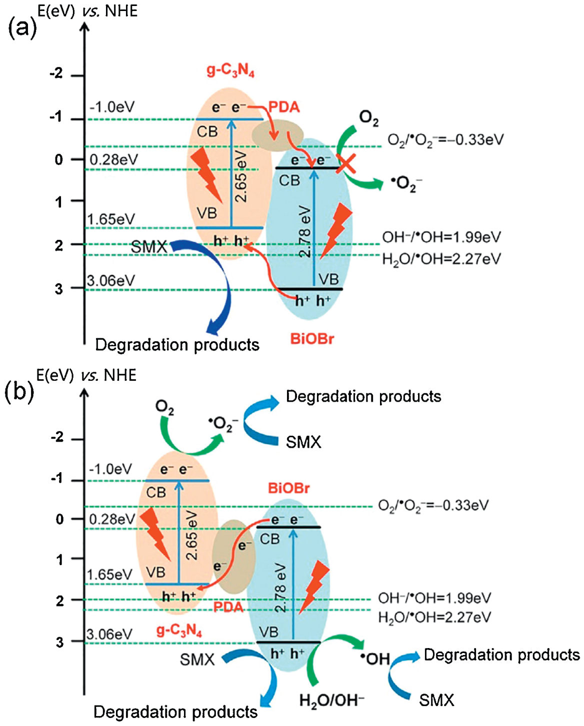

Fig. 7. Two possible mechanisms of charge transfer and photocatalytic degradation of SMX by CNPB under visible light irradiation. (a) traditional heterojunction-type and (b) Z-scheme type. Reproduced with permission [88]. Copyright 2020, Elsevier.

materials with CdS nanoparticles well dispersed at the high interface contact between ultra-thin BiOBr and $Bi_2O_2CO_3$ nanoplates [91]. The exposure of the composite to light led to the transfer of the photogenerated electrons in CB of BiOBr and $Bi_2O_2CO_3$ to the VB of CdS to finally recombine with the photogenerated holes. The photocatalytic reactions carried out at VB of (BiOBr and $Bi_2O_2CO_3$) and CB of CdS showed an increased photocatalytic activity by the double Z electron transfer process.

3.2.4. Construction of S-Scheme heterojunctions

A new type of step-scheme (S-scheme) heterojunction has recently been proposed by Yu *et al.* In this process, S-scheme heterojunctions consisting of both reduction and oxidation photocatalysts with staggered band structures were combined. For instance, Wang *et al.* synthesized Sb_2WO_6/BiOBr 2D nanocomposite S-scheme photocatalyst for NO removal. The photocatalytic mechanism suggested that both BiOBr and Sb_2WO_6 can be excited under visible-light irradiation to transfer excited electrons from CB of Sb_2WO_6 to the CB of BiOBr. Meanwhile, VB of Sb_2WO_6 received holes from the VB of BiOBr to induce a spatial charge separation with improved photocatalytic performances through efficient charge separation and limited electron-hole recombination [92]. Li *et al.* combined a facile liquid-phase ultrasound with a solvothermal method to prepare layered black phosphorus (BP)/BiOBr heterojunction. The coupling of chemical bonds between the interfaces yielded a large contact area and difference in Fermi energy level between the BiOBr and BP molecules, confirming the occurrence of S-scheme mechanism. Thanks to the internal electric field and band edge bending interaction, the relatively useless electrons from CB of BiOBr combined with the holes from VB of BP, while retaining useful charges with higher redox potentials [93].

A novel S-scheme heterojunction BiOBr/$BiO(CH_3COO)_{1-x}Br_x$ photocatalyst, in which $BiO(CH_3COO)_{1-x}Br_x$ and BiOBr acted as respectively reduced semiconductors with higher Fermi levels and oxidized photocatalysts with lower Fermi levels was produced by Jia *et al.* In this scheme, the contact between $BiO(CH_3COO)_{1-x}Br_x$ and BiOBr led to the formation of a heterojunction due to the differences in Fermi energy levels. This, in turn, induced an internal electric field at the BiOBr/$BiO(CH_3COO)_{1-x}Br_x$ interface. Under light irradiation, the relatively useless photoelectrons in CB of BiOBr migrated through the intimate interface to the VB of $BiO(CH_3COO)_{1-x}Br_x$, and then driven by the internal electric field to recombine with the relatively useless holes. The holes and electrons with high redox potentials were retained in VB of BiOBr and CB of $BiO(CH_3COO)_{1-x}Br_x$, respectively [94].

Meanwhile, the formation of a heterojunction scheme enhanced the photocatalytic performances by modulating the electrons and holes. Since BiOBr was often compounded with other semiconductor materials, more attention should thus be paid to matching the energy band structures of composite materials. The overall light absorption capacity should increase after recombination, and minimizing the loss of active sites would yield better BiOBr photocatalysts.

3.3. Engineering of surface states

After the migration of photogenerated electrons and holes from the bulk phase of the catalyst, photocatalytic reactions will take place on the surface. The electrons and holes will then react with the reactants adsorbed on the catalyst surface to finally complete the photocatalytic process. In other words, catalytic reactions on the surface consuming electrons and holes are charge separation processes. As a result, the adsorption of reactants and generation of charge transfer from bulk to the surface are considerably important in successful catalytic reactions. For BiOBr, its poor charge separation and positive CB potential are beneficial for its surface physical and chemical properties to reduce the recombination of electrons and holes on the surface and prolong their lifetime. This, in turn, will increase the probability of contact between electrons and holes of surface adsorbed reactants, leading to efficient photocatalytic reactions. In recent years, novel strategies based on the introduction of co-catalysts, surface modification, induction of defects, and exposure to crystal faces have been used to modulate the surface of BiOBr for enhanced charge separation and catalytic activity. These features are discussed below.

3.3.1. Loading of co-catalysts

Because of the poor catalytic ability of BiOBr, the separated electrons would require active sites for the photocatalytic reactions. This can be solved by the use of co-catalysts (usually metals or metallic compounds) to assist the electron-hole separation at the cocatalyst/semiconductor interface, as well as lower the activation energy [95]. In this regard, Mao *et al.* prepared a highly efficient and recoverable Ag/BiOBr-carboxymethyl cotton fabric photocatalytic composite material. The presence of noble metal Ag nanoparticles as co-catalysts reduced the efficiency of photogenic carriers as trapping centers of photogenic electrons, thereby improving the photocatalytic efficiency [96]. Huo *et al.* successfully deposited Ag/BiOBr thin film photocatalyst on a glass substrate. After reaching BiOBr surface, the photogenerated electrons migrated to the co-catalyst Ag surface, thereby declining the photoelectric charge and enhancing the photocatalytic activity [97].

3.3.2. Modification by polarized molecules

Surface modification is another way to enhance the charge separation since modifying molecules could induce polarization electric fields for electrons and holes migration. In this view, Jing *et al.* modified BiOBr nanoplates by phosphate groups to improve the O_2 adsorption. The characterization by various analytical techniques confirmed the efficacy of the phosphate modification route in improving the O_2 adsorption for capturing photogenerated electrons, as well as incrementing the charge separation. They also modified bismuth phosphate nanoparticles by controlling the amount of phosphate to enhance the charge separation generated by the formation of heterogeneous junctions [98]. Song *et al.* modified BiOBr by polar molecular 4-carboxythiophenolate anions (4CBT) to promote the formation of H_2O_2 absent in pure BiOBr suspension. The reason for this had to do with the polar surface induced by 4CBT modification that suppressed the excitonic effect and promoted the exciton dissociation into free electrons and holes [99]. Zhu *et al.* simultaneously modified BiOBr hierarchical spheres by phosphorylation and Bi by the solvothermal reaction in the presence of red phosphorus as additive. The synchronous phosphorylation and Bi modification of BiOBr improved the CO_2 conversion efficiency, especially the yield of CH_4 [100].

3.3.3. Engineering of surface defects

Surface defect engineering consists of manipulating the type, concentration, spatial distribution, or mobility of defects present on a crystalline semiconductor surface [101]. In other words, the presence of surface defects allows the modification of the microstructure, electronic structure, atomic coordination number, and charge transfer of an intrinsic semiconductor [102]. Numerous studies have so far demonstrated that engineering defects on BiOBr facilitated the charge separation and adsorption of reactants. For instance, Xue *et al.* synthesized an ultra-thin BiOBr nanosheet (thickness 4−8 nm) rich in oxygen vacancies (OVs). The photogenerated electrons in oxygen-containing vacancies of BiOBr nanosheets were captured by the OVs to participate in catalytic reactions, thereby inhibiting the recombination of electrons and holes. Meanwhile, the life of photogenerated carriers also prolonged and photocatalytic performances improved effectively [34]. Xia *et al.* prepared ultra-thin BiOBr nanosheets and successfully introduced Bi vacancies. Note that Bi vacancies could increment the charge density near the Fermi level, thereby enduring Bi vacancies BiOBr with more carriers to participate in catalytic processes. The existence of Bi vacancies also ensured higher carrier concentration and enhanced carrier transport, conducive to effectively enhancing the photocatalytic performances [103].

3.3.4. Exposure to specific crystal faces

Semiconductor photocatalysts possess specific exposed crystal surfaces useful for promoting the separation and transfer of photogenerated electron holes, as well as effectively improving the charge separation efficiency. Therefore, the specific exposed crystal surface could effectively be used as a method to improve the photocatalytic performances of semiconductor photocatalysts. For example, Scott *et al.* synthesized BiOBr-001 and BiOBr-010 particles with exposed (001) or (010) crystal faces using a simple chemical precipitation method. BiOBr-010 showed better photooxidation ability than BiOBr-001 in both water oxidation and water formic acid degradation. The higher photooxidation capacity of BiOBr-010 was attributed to the crystal surface with (010) place, which inhibited the recombination of photogenerated electron holes, promoted the charge transfer, effectively improved the separation efficiency of photogenerated electron holes, and enhanced the photooxidation activity [104]. Li *et al.* hydrothermally synthesized BiOBr-(001) and BiOBr-(010) nanosheets by adjusting the pH of the solution. The actual photoreactivity of BiOBr-(001) was found higher than that of BiOBr-(010) for both hydrogen production and oxygen evolution reactions. The unique photoreactivity was linked to highly exposed crystal faces, which cooperated with the co-exposed crystal faces to yield efficient spatial separation of the photogenerated charges. Also, the reduction and oxidation reactions occurred at different reaction rates on the dominant crystal plane and co-exposed crystal plane, respectively. Therefore, the photoreactivity of BiOBr nanosheets resulted from the balance between the reduction and oxidation reactions of different exposed crystal surfaces [14].

4. Applications in environmental remediation

4.1. Purification of pollutants

The very positive VB potential provides photogenerated holes with enough thermodynamic energy that can be used to oxidize organic pollutants. The holes may also oxidize water molecules into hydroxyl radicals suitable for oxidation. Despite the thermodynamically sluggish aspect of the O_2 activation by photoelectrons, the above-mentioned strategies efficiently enhance the charge separation and improve the photoactivity [105]. BiOBr-based photocatalysts have widely been used for the removal of pollutants, including ibuprofen [106], ciprofloxacin [107], ketoprofen [108], heavy metal mercury [90], aqueous Cr(VI) [109], NO [110], tetracycline hydrochloride [111], nocuous organic gases [25], atrazine [91] and carbamazepine [112].

4.1.1. Dyes degradation

Dye pollution has toxicity, carcinogenesis, and irreversible lesions on both the environment and human health. The discharge of dye compounds into water bodies restrict the passage of light to aquatic organisms, as well as increase the chemical and biochemical oxygen demand (COD and BOD), thereby deteriorating the environment and ecosystem. The photocatalytic degradation of dye compounds is advantageous in terms of green, environment-friendly, and high-efficiency. As a result, the concept attracted increasing interest in both academia and industry. For example, Kanagaraj *et al.* used the impregnation method to synthesize $SrTiO_3$-BiOBr heterojunction catalyst with different weight percentages. The as-obtained $SrTiO_3$ (10%)-BiOBr exhibited the lowest electron-hole recombination rate and lowest electron transfer resistance. Among prepared catalysts, the heterojunction catalyst $SrTiO_3$ (10%)-BiOBr exhibited the highest photocatalytic activity toward the degradation of reactive blue 198, reactive black 5, and reactive yellow 145. Under visible light irradiation, all dyes became decolorized within 20 min reaction time. During photocatalysis, the dyes were mineralized to form organic salts, such as acetate, formate, CO_2, and water [113]. Yang *et al.* successfully prepared a novel $LaFeO_3$/BiOBr heterojunction photocatalyst with Z-charge transfer mechanism. The activity of $LaFeO_3$ (20%)/BiOBr toward the degradation of rhodamine B (RhB) reached 21- and 1.3-fold those of bare $LaFeO_3$ nanoparticles and BiOBr microplates, respectively [114].

4.1.2. Degradation of medicinal molecules

The concentrations of some common drugs are increasing year after year in wastewater. To neutralize the toxicity of such drug pollutants to both the environment and human health, photocatalytic degradation processes have been extensively considered and used. In this view, Yu *et al.* synthesized Ag-BiOBr-reduced graphene oxide (rGO) photocatalyst, and studied its photocatalytic activity under visible light irradiation. Compared to other photocatalysts, Ag-BiOBr-rGO showed excellent photocatalytic activity and stability toward ketoffin degradation. Also, ketoprofen was completely cleared from wastewater samples in 120 min [108]. Wang *et al.* assembled a novel 3D flower-sphere BiOBr/$Bi_4O_5Br_2$ photocatalyst with ultra-high photocatalytic activity toward the antibiotic photodegradation of tetracycline and ciprofloxacin [115]. High mineralization ratesof ciprofloxacin (78%) and tetracycline (57%) after 100 min were observed. Xie *et al.* fabricated an economical and effective vessel-like biochar-based photocatalyst Bi_2S_3/BiOBr/BC through a facile solvothermal method [116]. The as-obtained photocatalyst displayed a good efficiency toward Diclofenac (DCF). Under visible light irradiation, the removal rate of DCF by Bi_2S_3/BiOBr/BC reached 93.65% in 40 min. The characterization experiments revealed that electrons transfer in biochar combined with high electrons and holes separation efficiencies were the reasons behind the improved degradation of DCF by Bi_2S_3/BiOBr/BC photocatalyst.

4.1.3. Removal of heavy metal

The bioaccumulation of heavy metals in the environment leads to toxicity to both the environment and human health. This can be alleviated by photocatalysis, which has been extensively studied. In this view, Wu *et al.* successfully synthesized a 3D BiOBr/$BiOIO_3$ Z-scheme heterojunction with abundant OVs and iodide ions by *in-situ* self-growth. During this process, 2D $BiOIO_3$ nanometer tablets could be grown uniformly on 3D BiOBr microspheres. The unique hierarchical structure of the resulting catalyst toward the adsorption of heavy metal mercury led to the enhanced optical response. As shown in Fig. 8, the existence of IO_3^-/I^- acted as an electronic medium to promote the separation and transfer of charge carriers. Meanwhile, carrier migration consisting of Z-scheme heterojunctions and OVs in BiOBr/$BiOIO_3$ did not only promote the efficiency of electron-hole pair separation and transfer but also retained the occurrence of efficient redox reactions. Consequently, BiOBr/$BiOIO_3$ displayed high photocatalytic activity toward the removal of heavy metal mercury in flue gas under visible-light reaching up 90.25% [90]. Luo *et al.* synthesized Z-scheme rGO/Bi_2S_3-BiOBr heterojunction photocatalyst using a one-pot solvothermal strategy. The Z-scheme reduced rGO/Bi_2S_3-BiOBr heterojunction with a tunable exposed BiOBr (102) facet and

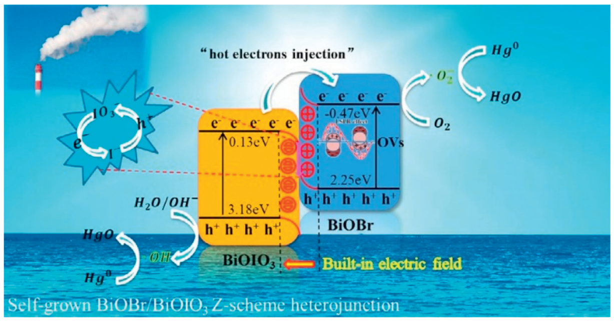

Fig. 8. The schematic diagram of possible charge separation mechanism for direct Z-scheme BiOBr/$BiOIO_3$ nanocomposite under visible-light irradiation. Reproduced with permission [90]. Copyright 2020, Elsevier.

high stability toward reduction of 2-nitrophenol (2NP) and degradation of Cr(VI) in solution [117]. The Cr(VI) reduction and 2NP degradation efficiencies reached 95% and 67%, respectively.

4.2. CO_2 reduction

The large amounts of carbon dioxide (CO_2) emitted by burning fossil fuels has led to considerable global warming [118]. Therefore, the reduction of CO_2 into usable carbon products through sustainable solar energy is an attractive way to solve currents energy problems and reduce the greenhouse effect. Under light irradiation, CO_2 molecules in the presence of appropriate photocatalysts and H_2O could be reduced to form CO, HCHO, HCOOH, CH_3OH, CH_4, and C_2H_5OH [95]. Among photocatalysts, BiOBr is a non-toxic layered semiconductor with a good visible light response. However, the positive CB potential of BiOBr makes it thermodynamically insufficient for reducing CO_2. To improve the activity of BiOBr toward CO_2 reduction, several efficient methods have been developed through the formation of vacancies and dopants. For example, Bi vacancy-tuned BiOBr ultrathin nanosheets were successfully prepared by controlling the synthesis of 1-hexadecyl-3-methyl-imidazolium bromine ([C16mim]Br) ionic liquid-assisted at room temperature to reduce CO_2 into CO [103]. The Bi vacancy-tuned BiOBr ultrathin nanosheets showed a highly selective carbon monoxide production rate of 20.1 μmol g^{-1} h^{-1}, equivalent to 3.8-fold that of BiOBr ultrathin nanosheets. Xie *et al.* *in-situ* doped Gd^{3+} into BiOBr microspheres consisting of nanosheets *via* a simple hydrothermal method. Compared to pure BiOBr, the Gd-doped BiOBr photocatalyst showed outstanding performances toward the CO_2 reduction with a nearly 5-fold increase in the rate of methanol generation. The enhanced CO_2 photoreduction activities of Gd-doped BiOBr photocatalyst was attributed to the mingling of Gd^{3+} ions into the lattice of BiOBr to broaden its visible light response during CO_2 reduction [119]. However, the efficiencies of CO_2 reduction by existing BiOBr photocatalysts are still low despite advances in synthesis methods, thereby require future studies.

4.3. Other applications

In addition to the above-mentioned applications, BiOBr-based photocatalysts have also been used in other fields. In this regard, Liu *et al.* synthesized a BiOBr/g-C_3N_4 heterojunction with surface OVs by a simple solvothermal method withremoval rate by photocatalytic oxidation of NO reaching 63%. Their data revealed that the heterojunction boosted the transfer and separation efficiency of photogenerated electrons and holes, in which surface OVs increased the capture of photoinduced electrons on the catalyst surface [120]. Wang *et al.* fabricated a novel oxygen-rich vacancy ultrathin sulfur-doped BiOBr nanosheet by a simple one-step solvent-thermal synthesis route. Under visible-light irradiation, the degradation efficiency of 4-chlorophenol (4-CP) by the optimized catalyst reached 98% within 2 h, a value 4.9- and 18.0-fold higher than those obtained by sulfur-doped and bulk BiOBr, respectively. Furthermore, the excellent photoactivity was extended to other colorless organic pollutants, such as bisphenol analogs and sulfonamides [121].

The practical utilization of photocatalysis in environmental remediation is highly desirable. Recently, practical photocatalysis has been carried out to lower pollutants levels in the air with excellent performance [122]. BiOBr materials have also been used as photocatalysts in wastewater treatment. Shi *et al.* synthesized

Table 2
Applications of BiOBr photocatalysts in environmental remediation.

Sample	Synthesis method	Morphology	Application	Photocatalytic activity	Ref
$SrTiO_3$ (10%)-BiOBr	Precipitation	Flower-like structures	Degradation of reactive blue 198, reactive black 5, and reactive yellow 145.	$SrTiO_3$ (10%)-BiOBr > BiOBr > $SrTiO_3$.	[113]
$LaFeO_3$ (20%)/BiOBr	Hydrothermal	Microplates	Degradation of RhB.	Values 21.0- and 1.3-fold larger than bare $LaFeO_3$ nanoparticles and BiOBr microplates, respectively.	[114]
Ag-BiOBr-rGO	Solvothermal	Flower-like microstructures	Degradation of ketoprofen.	Complete removal in 120 min.	[108]
BiOBr/$Bi_4O_5Br_2$	Solvothermal	3D flower-spheres	Photodegradation of tetracycline and ciprofloxacin.	High mineralization rate of ciprofloxacin (78%) and tetracycline (57%) after 100 min.	[115]
Bi_2S_3/BiOBr/BC	Solvothermal	Rough blocks	Removal of diclofenac.	Removal with 93.65% in 120 min.	[116]
BiOBr/$BiOIO_3$	Solvothermal	Microspheres	Removal of heavy metal mercury.	Removal with 90.25% efficiency.	[102]
rGO/Bi_2S_3-BiOBr	Solvothermal	Irregular agglomeration of nano-sheets	Reduction of 2NP and degradation of Cr(VI).	Cr(VI) reduction and 2NP degradation efficiencies reaching 95% and 67%, respectively.	[117]
Bi vacancy-tuned BiOBr	Precipitation	Nanosheets	CO_2 reduction.	3.8-fold higher than BiOBr nanosheets.	[103]
Gd-doped BiOBr	Hydrothermal	Microspheres	CO_2 reduction.	5-fold higher than BiOB.	[119]
BiOBr/g-C_3N_4	Solvothermal	Nanoflowers	Photocatalytic oxidation of NO.	Removal rate of 63%.	[120]
sulfur-doped BiOBr	Solvothermal	Nanosheets	Degradation of 4-CP.	Removal rate of 98% within 2 h.	[121]
BiOBr-OV	Solvothermal	Nanosheets	Treatment of oilfield production wastewater.	COD reduction rate twice that BiOBr.	[123]

multilayer BiOBr-OV nanosheets composed of ultrathin nanosheets with OVs. Under light stimulation, part of the photogenerated electrons was captured by OVs, effectively promoting the separation of the photogenerated electron holes. Meanwhile, O_2 reacted with captured photogenerated electrons to produce $^{\bullet}O_2^-$, and some $^{\bullet}O_2^-$ reacted with photogenerated holes to generate singlet oxygen ($^1O_2$). The enhanced $^1O_2$ and $^{\bullet}O_2^-$ generated by the capture of electrons by OVs in the photocatalytic process efficiently incremented the photocatalytic performance of BiOBr-OV. The COD value of oilfield production wastewater reduced from 18,900 mg/L to 6800 mg/L after 5 h of BiOBr-OV treatment, and COD reduction rate was about twice that of BiOBr. Thus, BiOBr-OV showed higher photocatalytic efficiency [123].

Table 2 lists the applications of BiOBr photocatalysts. It is clear that BiOBr photocatalysts can be applied in many fields of the environment.

5. Summary and future outlooks

BiOBr-based materials are promising photocatalysts for environmental remediation. As a result, the BiOBr structure in terms of electronic, crystalline, and dimensional-based morphology were all reviewed and discussed to gain a better understanding and provide good guidance for future studies. Different synthetic methods of BiOBr were then introduced, including the hydrothermal and solvothermal routes, as well as the hydrolytic precipitation and microwave assistant strategies. These methods were found efficient in controlling the morphologies and modulating the vacancies of BiOBr. The strategies for enhancing the charge separation were also discussed, including the preparation of ultrathin 2D structures for bulk charge transfer, construction of heterojunction nanocomposites for photoelectron modulation, surface engineering of coupling co-catalysts, and creation of surface polarization and tuning defects. Finally, the applications of BiOBr-based photocatalysts in pollutants degradation and CO_2 reduction were all summarized and discussed.

Despite the significant progress, more efforts are still required to further explore the advantages of BiOBr-based photocatalysts in environmental remediation. The following outlooks deserve research attention:

(1) With a light absorption edge around 460 nm, the visible-light response of BiOBr is still limited. Though doping methods can narrow the bandgap and improve visible-light response, the poor stability and lost thermodynamic energy could have adverse effects on the activity. In terms of the electronic structure of BiOBr, tuning the ratios of Bi, O and Br during the synthesis of Bi-rich or O-rich BiOBr materials like $Bi_4O_5Br_2$ and Bi_3O_4Br could be an effective approach.

(2) The charge separation remains challenging in gaining high photoactivity of BiOBr-based materials. Coupling wide bandgap oxides like TiO_2 and SnO_2 are effective for enhancing the charge separation, by transferring the visible-light-excited photoelectrons in high energy levels of CB to drive the charge separation and maintain the thermodynamic energy. In this case, searching for appropriate semiconductors with reasonable bandgaps and CB potentials would help construct high-quality interfaces with BiOBr. Additionally, the construction of heterogeneous junctions like type II, Z-scheme and S-scheme may improve the light absorption and charge separation. Some organic semiconductors and molecular photocatalysts, such as g-C_3N_4, phthalocyanine metals, metalloporphyrins and covalent organic frameworks are great candidates due to their narrowed bandgaps and very negative CB bottoms. On the one hand, the polarization fields formed by polar semiconductor materials under spontaneous polarization, external stress, or electric field drove the photogenerated electrons and holes to the opposite electrode, effectively promoting the charge separation and greatly enhancing the photocatalytic reaction activity. Therefore, BiOBr with layered structure was also expected to promote the charge separation through the construction of the polarization field. On the other hand, in-depth understanding of the photophysical processes like charge transfer, band bending and carrier kinetic would help and can be done by time-resolution ultrafast spectroscopy, *in-situ* techniques, and theoretical calculations.

(3) The insufficient surface catalytic capacity of BiOBr photocatalyst leads to charge recombination and poor activity. Thus, creating more catalytic sites on BiOBr would be effective for improving the photocatalytic activities. OVs with abundant local electronic states have strong adsorption abilities and activation capacities of reactants. However, an in-depth understanding of the relationship between defect types, quantity, and photocatalytic performance is missing and require future investigations. Hence, controlling the number of defects and ratio of multiple defects during catalyst design combined with the evaluation of the properties should enhance the photocatalytic performances.

(4) Extending the applications of BiOBr-based photocatalysts is meaningful to the development of visible-light photocatalysis. The dual function in the environment and energy can be achieved by holes for oxidizing pollutants and electrons to produce H_2. Bi ions with empty orbitals are easy to expose on the surface of BiOBr, leading to the high selectivity of reactants with long pair electrons. The selectivity of holes induced reactions would form separated electrons for better reduction processes. This makes BiOBr useful for dual function in the environment and energy.

Declaration of competing interest

The authors report no declarations of interest.

Acknowledgments

The authors are grateful for the financial supports from the National Natural Science Foundation of China project (Nos. 21971057, U1805255), Outstanding Youth Project of Natural Science Foundation of Heilongjiang Province (No. YQ2019B006), and Postdoctoral Research Foundation of Heilongjiang Province (Nos. LBH-Q19052 and 2020-KYYWF-1008).

References

[1] A. Kumar, S.K. Sharma, G. Sharma, et al., J. Hazard. Mater. 364 (2019) 429–440.
[2] M. Cybularczyk-Cecotka, J. Szczepanik, M. Giedyk, Nat. Catal. 3 (2020) 872–886.
[3] M. Pálmai, E.M. Zahran, S. Angaramo, et al., J. Mater. Chem. A 2 (2017) 529–534.
[4] T.X. Xu, J.P. Wang, Y. Cong, et al., Chin. Chem. Lett. 31 (2020) 1022–1025.
[5] H. Song, X.G. Meng, S.Y. Wang, et al., J. Am. Chem. Soc. 141 (2019) 20507–20515.
[6] F. You, J.W. Wan, J. Qi, et al., Angew. Chem. 132 (2020) 731–734.
[7] D.W. Su, J. Ran, Z.W. Zhuang, et al., Sci. Adv. 6 (2020) eaaz8447.
[8] Y. Wang, Z.Z. Zhang, L.N. Zhang, et al., J. Am. Chem. Soc. 140 (2018) 14595–14598.
[9] S. Song, J.F. Qu, P.J. Han, et al., Nat. Commun. 11 (2020) 1–10.
[10] J.L. He, W.H. Fang, R. Long, O.V. Prezhdo, J. Am. Chem. Soc. 141 (2019) 5798–5807.
[11] S. Nadupalli, J. Kreisel, T. Granzow, Sci. Adv. 5 (2019) eaau9199.
[12] Y.Z. Wei, J.Y. Wang, R.B. Yu, J.W. Wan, D. Wang, Angew. Chem. In. Ed. 58 (2019) 1422–1426.
[13] J.Z. Liao, K.L. Li, H. Ma, et al., Chin. Chem. Lett. 31 (2020) 2737–2741.
[14] M. Shi, G.N. Li, J.M. Li, et al., Angew. Chem. In. Ed. 59 (2020) 6590–6595.
[15] M.D. Sun, Z.M. Zhang, Q.J. Shi, et al., Chin. Chem. Lett. 32 (2021) 2419–2422.
[16] J.D. Hu, D.Y. Chen, Z. Mo, et al., Angew. Chem. Int. Ed. 58 (2019) 2073–2077.

[17] Y.C. Zhou, P. Wang, H.F. Fu, C. Zhao, C.C. Wang, Chin. Chem. Lett. 31 (2020) 2645–2650.
[18] J. Kim, S.H. Lee, F. Tieves, et al., Sci. Adv. 5 (2019) eaax0501.
[19] F. Chen, H.W. Huang, Y.H. Zhang, T.R. Zhang, Chin. Chem. Lett. 28 (2017) 2244–2250.
[20] F. Yang, Y. Qu, L.Q. Jing, Chin. Chem. Lett. 3 (2020) 2784–2788.
[21] X.Q. Li, J.D. Wang, Z.M. Hu, M.J. Li, K. Ogino, Chin. Chem. Lett. 29 (2018) 166–170.
[22] Y. Zhang, J. Guo, L. Shi, et al., Sci. Adv. 3 (2017) e1701162.
[23] X.Y. Wang, L.J. Chen, S.Y. Chong, et al., Nat. Chem. 10 (2018) 1180–1189.
[24] Y.W. Huang, N. Zhang, Z.J. Wu, X.Q. Xie, J. Mater. Chem. A 8 (2020) 4978–4995.
[25] S.R. Kim, W.K. Jo, J. Hazard. Mater. 380 (2019) 120866.
[26] L.L. Liang, S.W. Gao, J.C. Zhu, et al., Chem. Eng. J. 391 (2020) 123599.
[27] H. Wang, D.Y. Yong, S.C. Chen, et al., J. Am. Chem. Soc. 140 (2018) 1760–1766.
[28] M.H. Guan, G.M. Ren, X.C. Zhang, et al., Int. J. Quantum Chem. (2020) e26568.
[29] Z.Y. Zhao, W.W. Dai, Inorg. Chem. 53 (2014) 13001–13011.
[30] L.Q. Ye, Y.R. Su, X.L. Jin, H.Q. Xie, C. Zhang, Environ. Sci. Nano 1 (2014) 90–112.
[31] S.J. Zhang, X.X. Chen, L.M. Song, J. Hazard. Mater. 367 (2019) 304–315.
[32] J. Wu, X.D. Li, W. Shi, et al., Angew. Chem. In. Ed. 130 (2018) 8855–8859.
[33] J. Li, H. Li, G.M. Zhan, L.Z. Zhang, Acc. Chem. Res. 50 (2017) 112–121.
[34] X.L. Xue, R.P. Chen, H.W. Chen, et al., Nano Lett. 18 (2018) 7372–7377.
[35] T. Li, Y.W. Gao, L.Z. Zhang, et al., Appl. Catal. B: Environ. 277 (2020) 119065.
[36] X. Zhang, Z.H. Ai, F.L. Jia, L.Z. Zhang, J. Phys. Chem. C 112 (2008) 747–753.
[37] W.D. Wang, F.Q. Huang, X.P. Lin, Jh. Yang, Catal. Commun. 9 (2008) 8–12.
[38] H.F. Cheng, B.B. Huang, Y. Dai, Nanoscale 6 (2014) 2009–2026.
[39] J. Di, J.X. Xia, H.M. Li, S.J. Guo, S. Dai, Nano Energy 41 (2017) 172–192.
[40] X.L. Wu, C.Y. Toe, C.L. Su, et al., J. Mater. Chem. A 8 (2020) 15302–15318.
[41] L.P. Han, Y.X. Guo, Z. Lin, H.W. Huang, Colloids Surf. A 603 (2020) 125233.
[42] W.D. Shi, S.Y. Song, H.J. Zhang, Chem. Soc. Rev. 42 (2013) 5714–5743.
[43] P. Basnet, S. Chatterjee, Nano-Struct. Nano-Objects 22 (2020) 100426.
[44] D. Wu, S.T. Yue, W. Wang, et al., Appl. Catal. B: Environ. 192 (2016) 35–45.
[45] Y.X. Guo, I. Siretanu, Y.H. Zhang, et al., J. Mater. Chem. A 6 (2018) 7500–7508.
[46] D. Wu, B. Wang, W. Wang, et al., J. Mater. Chem. A 3 (2015) 15148–15155.
[47] Z. Fan, Y.B. Zhao, W. Zhai, et al., RSC Adv. 6 (2016) 2028–2031.
[48] A.J. Han, H.W. Zhang, G.K. Chuah, S. Jaenicke, Appl. Catal. B: Environ. 219 (2017) 269–275.
[49] J.P. Lai, W.X. Niu, R. Luque, G.B. Xu, Nano Today 10 (2015) 240–267.
[50] Y.N. Huo, J. Zhang, M. Miao, Y. Jin, Appl. Catal. B: Environ. 111-112 (2012) 334–341.
[51] L.L. Chang, Y.P. Pu, G.D. Shen, et al., New J. Chem. 44 (2020) 2479–2488.
[52] X.C. Lv, D.Y.S. Yan, F.L.Y. Lam, et al., Chem. Eng. J. 401 (2020) 126012.
[53] Y.X. Yang, L. Geng, Y.H. Guo, Y.N. Guo, J. Chem, Technol. Biotechnol. 92 (2017) 1236–1247.
[54] Y. Zhao, T. Yu, X. Tan, C. Xie, S.C. Wang, Dalton Trans. 44 (2015) 20475–20483.
[55] D. Zhang, J. Li, Q.G. Wang, Q.S. Wu, J. Mater. Chem. A 1 (2013) 8622–8629.
[56] L.L. Zhang, X.P. Yue, J.X. Liu, et al., Sep. Purif. Technol. 231 (2020) 115917.
[57] K. Li, H.B. Zhang, Y.P. Tang, et al., Appl. Catal. B: Environ. 164 (2015) 82–91.
[58] X.J. Yu, H.R. Qiu, B. Wang, et al., J. Alloys Compd. 839 (2020) 155597.
[59] X.Y. Wu, K.K. Zhang, G.K. Zhan, S. Yin, Chem. Eng. J. 352 (2017) 59–70.
[60] W.D. Zhang, Q. Zhang, F. Dong, Ind. Eng. Chem. Res. 52 (2013) 6740–6746.
[61] Z.H. Ai, W.K. Ho, S.C. Lee, L.Z. Zhang, Environ. Sci. Technol. 43 (2009) 4143–4150.
[62] Y.T. Cai, J. Song, X.Y. Liu, et al., Environ. Sci. Nano 5 (2018) 2631–2640.
[63] G.F. Li, F. Qin, R.M. Wang, et al., J. Colloid Interf. Sci. 409 (2013) 43–51.
[64] Y.C. Miao, Z.C. Lian, Y.N. Huo, H.X. Li, Chin. J. Catal. 39 (2018) 1411–1417.
[65] J. Li, L.J. Cai, J. Shang, Y. Yu, L.Z. Zhang, Adv. Mater. 28 (2016) 4059–4064.
[66] Y.X. Zhao, S. Zhang, R. Shi, et al., Mater. Today 34 (2020) 78–91.
[67] J. Di, J.X. Xia, M.X. Ji, et al., ACS Sustain. Chem. Eng. 4 (2016) 136–146.
[68] Q. Jiang, M.X. Ji, R. Chen, et al., J. Colloid Interf. Sci. 574 (2020) 131–139.
[69] Z.D. Wang, Z. Chu, C.W. Dong, et al., ACS Appl. Nano Mater. 3 (2020) 1981–1991.
[70] S. Patnaik, D.P. Sahoo, K. Parida, Carbon 172 (2021) 682–711.
[71] J.J. Jiang, G. Ye, Z. Wang, et al., Angew. Chem. Int. Ed. 57 (2018) 12037–12042.
[72] I. Shown, S. Samireddi, Y.C. Chang, et al., Nat. Commun. 9 (2018) 1–10.
[73] D.X. Yang, J.L. Liang, L. Luo, et al., Chin. Chem. Lett. 32 (2021) 2534–2538.
[74] L.H. Shao, Y.T. Liu, L.L. Wang, X.N. Xia, X.Y. Shen, Appl. Surf. Sci. 502 (2020) 143895.
[75] W. Wang, R. Dai, L. Zhang, et al., J. Mater. Sci. 55 (2020) 11226–11240.
[76] J.Q. Guo, X. Liao, M.H. Lee, et al., Appl. Catal. B: Environ. 243 (2019) 502–512.
[77] X.C. Jiao, K. Zheng, L. Liang, et al., Chem. Soc. Rev. 49 (2020) 6592–6604.
[78] K. Sharma, V. Dutta, S. Sharma, et al., J. Ind. Eng. Chem. 78 (2019) 1–20.
[79] Y. Wang, Y. Long, Z.Q. Yang, D. Zhang, J. Hazard. Mater. 351 (2018) 11–19.
[80] Z. Shi, Y. Zhang, X.F. Shen, et al., Chem. Eng. J. 386 (2020) 124010.
[81] C.S. Guo, S.W. Gao, J.P. Lv, et al., Appl. Catal. B: Environ. 205 (2017) 68–77.
[82] Z.Q. Zhang, L.L. Bai, Z.J. Li, Y. Qu, L.Q. Jing, J. Mater. Chem. A 7 (2019) 10879–10897.
[83] H. Wang, Y. Qu, Z.K. Xu, et al., Sci. China Mater. 62 (2019) 653–661.
[84] H.Z. Wu, C.W. Yuan, R.M. Chen, et al., ACS Appl. Mater. Interfaces 12 (2020) 43741–43749.
[85] L.S. Jiang, Y. Xie, F. He, et al., Chin. Chem. Lett. 32 (2021) 2187–2191.
[86] V. Dutta, S. Sharma, P. Raizada, et al., J. Environ. Chem. Eng. 8 (2020) 104505.
[87] T. Jia, J. Wu, Y. Xiao, et al., J. Colloid Interf. Sci. 587 (2021) 402–416.
[88] F.R. Guo, J.C. Chen, J.Z. Zhao, et al., Chem. Eng. J. 386 (2020) 124014.
[89] J.C. Sin, S.M. Lam, H.H. Zeng, et al., Sep. Purif. Technol. 250 (2020) 117186.
[90] T. Jia, J. Wu, J. Song, et al., Chem. Eng. J. 396 (2020) 125258.
[91] D. Majhi, K. Das, A. Mishra, R. Dhiman, B.G. Mishra, Appl. Catal. B: Environ. 260 (2020) 118222.
[92] Y.Y. Wang, K. Wang, J.L. Wang, X.Y. Wu, G.K. Zhang, J. Mater. Sci. Technol. 56 (2020) 236–243.
[93] X.B. Li, J. Xiong, X.M. Gao, et al., J. Hazard. Mater. 387 (2020) 121690.
[94] X.X. Jia, Q.F. Han, H.Z. Liu, S.Z. Li, H.P. Bi, Chem. Eng. J. 399 (2020) 125701.
[95] L.Q. Ye, Y. Deng, L. Wang, H.Q. Xie, F.Y. Su, ChemSusChem 12 (2019) 3671–3701.
[96] P.W. Zhou, L.P. Zhang, Y.M. Dai, et al., J. Clean. Prod. 246 (2020) 119007.
[97] H.B. Yin, X.F. Chen, R.J. Hou, et al., ACS Appl. Mater. Interfaces 7 (2015) 20076–20082.
[98] S.Y. Chen, R. Yan, X.L. Zhang, et al., Appl. Catal. B: Environ. 209 (2017) 320–328.
[99] X.H. Song, J.J. Wang, R.Q. Zhang, et al., J. Phys. Chem. C 123 (2019) 15599–15605.
[100] J.Y. Zhu, Y.P. Li, X.J. Wang, et al., ACS Sustain. Chem. Eng. 7 (2019) 14953–14961.
[101] F. Chen, T.Y. Ma, T.R. Zhang, Y.H. Zhang, H.W. Huang, Adv. Mater. 33 (2021) 2005256.
[102] F. Chen, Z.Y. Ma, L.Q. Ye, et al., Adv. Mater. 32 (2020) 1908350.
[103] J. Di, C. Chen, C. Zhu, et al., ACS Appl. Mater. Interfaces 11 (2019) 30786–30792.
[104] X.L. Wu, Y.H. Ng, L. Wang, et al., J. Mater. Chem. A 5 (2017) 8117–8124.
[105] F. Yang, X.Y. Chu, J.H. Sun, et al., Chin. Chem. Lett. 31 (2020) 2784–2788.
[106] M. Khan, C.S.L. Fung, A. Kumar, I.M.C. Lo, J. Hazard. Mater. 365 (2019) 733–743.
[107] J. Di, J.X. Xia, M.X. Ji, et al., J. Mater. Chem. A 3 (2015) 15108–15118.
[108] G.H. Xu, M. Li, Y. Wang, et al., Sci. Total Environ. 678 (2019) 173–180.
[109] L.X. Jia, W. Zhou, X. Huang, et al., Environ. Sci. Nano 6 (2019) 3601–3610.
[110] X. Shi, P.Q. Wang, W. Li, et al., Appl. Catal. B: Environ. 243 (2019) 322–329.
[111] X.R. Yang, Z. Chen, W. Zhao, et al., J. Alloys Compd. 864 (2021) 158784.
[112] B.C. Hodges, E.L. Cates, J.H. Kim, Nat. Nanotechnol. 13 (2018) 642–650.
[113] T. Kanagaraj, S. Thiripuranthagan, Appl. Catal. B: Environ. 207 (2017) 218–232.
[114] S.T. Guan, H. Yang, X.F. Sun, T. Xian, Opt. Mater. 100 (2020) 109644.
[115] P.J. Li, W. Cao, Y. Zhu, et al., Sci. Total Environ. 715 (2020) 136809.
[116] S. Li, Z.R. Wang, X.Y. Xie, et al., J. Hazard. Mater. 391 (2020) 121407.
[117] H. Li, F. Deng, Y. Zheng, et al., Environ. Sci. Nano 6 (2019) 3670–3683.
[118] S.B. Wang, X. Han, Y.H. Zhang, et al., Small Struct. 2 (2021) 2000061.
[119] J. Wu, Y. Xie, Y. Ling, et al., Chem. Eng. J. 400 (2020) 125944.
[120] D.N. Liu, D.Y. Chen, N.J. Li, et al., Angew. Chem. 132 (2020) 4549–4554.
[121] Q. Wang, Z.Q. Liu, D.M. Liu, et al., Chem. Eng. J. 360 (2019) 838–847.
[122] Y. Huang, J. Zhang, Z.Y. Wang, et al., Sol. RRL 4 (2020) 2000170.
[123] X. Shi, P.Q. Wang, L. Wang, et al., ACS Sustain. Chem. Eng. 6 (2018) 13739–13746.